Performance of the OPA/ARPEGE-T21 global ocean-atmosphere coupled model

E. Guilyardi[1] and G. Madec[2]

[1] Climate Modelling and Global Change, CERFACS, 42, avenue Gustave Coriolis, 31057 Toulouse cedex, France
[2] Laboratoire d'Océanographie DYnamique et de Climatologie (CNRS/UPMC/ORSTOM), Université Paris VI, Case 100, 4 place Jussieu, 75252 Paris cedex 05, France

Abstract. The climatology of the OPA/ARPEGE-T21 coupled general circulation model (GCM) is presented. The atmosphere GCM has a T21 spectral truncation and the ocean GCM has a $2° \times 1.5°$ average resolution. A 50-year climatic simulation is performed using the OASIS coupler, without flux correction techniques. The mean state and seasonal cycle for the last 10 years of the experiment are described and compared to the corresponding uncoupled experiments and to climatology when available. The model reasonably simulates most of the basic features of the observed climate. Energy budgets and transports in the coupled system, of importance for climate studies, are assessed and prove to be within available estimates. After an adjustment phase of a few years, the model stabilizes around a mean state where the tropics are warm and resemble a permanent ENSO, the Southern Ocean warms and almost no sea-ice is left in the Southern Hemisphere. The atmospheric circulation becomes more zonal and symmetric with respect to the equator. Once those systematic errors are established, the model shows little secular drift, the small remaining trends being mainly associated to horizontal physics in the ocean GCM. The stability of the model is shown to be related to qualities already present in the uncoupled GCMs used, namely a balanced radiation budget at the top-of-the-atmosphere and a tight ocean thermocline.

1 Introduction

The study of present-day climate variability on time scales ranging from interannual to inter-decadal is one of the main interest of the climate research community. After the pioneering work of Manabe and Bryan (1969), a first generation of coupled general circulation models (GCM) was designed to address global change issues (Manabe et al. 1991; 1992, Cubasch et al. 1992; Washington and Meehl 1989; Murphy 1992; review by Meehl 1990). These coarse resolution models were initially subject to spurious climate drifts (see intercomparison by Gates et al. 1993). Two major causes were identified: a lack of equilibrium of the ocean (which is the main *memory* of the coupled system) and deficient air-sea fluxes. Attempts to correct the former led to *spin-up* techniques during which the ocean model was integrated alone towards equilibrium, using either observed or atmosphere GCM fluxes, the resulting mean state being usually different from the observed one. The latter was reduced by the use of surface flux correction techniques (Stockdale et al. 1994; Murphy 1995; Meehl 1995).

Nevertheless, such techniques have non-negligible drawbacks. Indeed, climate variability can be seen as anomaly departures from a mean state. If such anomalies in the oceanic and atmospheric fields interact non-linearly with the mean values, the dependence of natural climate variability on the mean state of the system is likely to be important. Therefore, the study of present-day climate variability requires the initial mean state of the coupled system to be close to the observed one. Several authors investigated the effect of surface flux correction on the coupled models results (Meehl 1995; Murphy 1995; Neelin and Dijkstra 1995) and concluded that the effects of these artificial corrections on the model variability were unclear. Here, we wish to assess present-day climate variability. Hence, the initial oceanic state needs to be as close as possible to observations and no flux correction technique is to be used at the air-sea interface. The resulting climate drift(s) will point out the deficiencies of the coupled model physical parametrizations and will suggest refinements for further development in model formulation and modelling assumptions.

In this perspective, the OPA-ARPEGE coupled model is developed as part of the French climate community effort to study climate variability and potential anthropogenic effects. This research group, called GASTON, involves CERFACS (Centre Européen de Recherche et de Formation Avancée en Calcul Scientifique), CNRM (Centre National de Recherches Météorologiques, Météo

Correspondence to: E. Guilyardi

France), LMCE (Laboratoire de Modélisation du Climat et de l'Environement, CEA-IPSL), LMD (Laboratoire de Météorologie Dynamique, CNRS-IPSL) and LODYC (Laboratorie d'Océanographie DYnamique et de Climatologie, CNRS/UPMC/ORSTOM-IPSL) and provides two atmosphere GCMs: ARPEGE-climat (Déqué et al. 1994) and LMD (Sadourny and Laval 1984; Letreut et al. 1994) and one ocean GCM : OPA (Delecluse et al. 1993) which are coupled together through the same coupling tools OASIS (Terray 1994), using different model resolutions. Each model is developed on its own grid (best suited to its physical and numerical requirements) and the OASIS coupler permits the exchanges between the quite different grids involved.

In this study, we present the climatology of a first 50-year long simulation performed with the OPA/AR-PEGE-T21 coupled model (Guilyardi et al. 1995). It involves a low resolution atmospheric model (T21) coupled to a $2 \times 1.5°$ average resolution oceanic model. The emphasis is put on global and integral diagnostics in order to document its main climatological features. Comparison to the corresponding uncoupled experiments points out the effect of the coupling on the realistic/unrealistic features already present in each component. Several regional climate drifts are analyzed as they give an insight into the shortcomings of some of the model physical parametrizations.

The model components and the experimental design are described in Sect. 2. Section 3 presents the climatology of the simulation, including a global energy budget. We discuss the global-scale characteristics of the simulation and analyse several regional deficiencies in Sect. 4. We conclude the paper in Sect. 5 with a summary and some directions for future work.

2 Model description and experimental design

2.1 The ARPEGE model

The ARPEGE-climat (Version 1) atmosphere GCM, from CNRM/Météo-France, is a state-of-the-art spectral atmosphere model developed from the ARPEGE/IFS weather forecast model (Déqué et al. 1994). The model has 30 vertical levels extending up to 70 km (0.02 hPa). A triangular spectral T21 truncation has been used for horizontal resolution corresponding to a 5.6° grid size. The radiation scheme is both an extension and a simplification of the methods described in Geleyn and Hollingsworth (1979) with optical properties synthesized using a few coefficients following methods similar to those of Ritter and Geleyn (1991). Both deep and shallow convection are parametrized. The deep convection uses a mass-flux scheme with detrainment described by Bougeault (1985) while the shallow convection is parametrized with a modified Richardson number scheme described by Geleyn (1987). The exchange and drag coefficients for heat and momentum are computed according to Louis et al. (1982). Convective and stratiform cloudiness are calculated using respectively the precipitation rates and the vertical humidity profile. A two-layer prognostic soil temperature

scheme is included in the model, the deeper temperature being restored towards a climatological estimate. The time step is 30 minutes. This model is part of the AMIP (Atmospheric Model Intercomparison Project) intercomparison (Gates 1992) and has been used for sensitivity studies including the removal of Arctic sea ice (Royer et al. 1990) and time slice experiments (Mahfouf et al. 1994; Timbal et al. 1995).

2.2 The OPA model

The OPA ocean GCM has been developed at the Laboratoire d'Océanographie Dynamique et de Climatologie (LODYC) (Delecluse et al. 1993). It has been used at levels from process studies (Madec et al. 1991) to basin- (Reverdin et al. 1991; Blanke and Delecluse 1993; Dandin 1993) and global-scale studies (Madec and Imbard 1996). It solves the primitive equations with a non-linear equation of state (Unesco 1983). A rigid lid is assumed at the sea surface. The code has been adapted to the global ocean by Madec and Imbard (1996). The horizontal mesh is orthogonal and curvilinear on the sphere. It does not have a geographical configuration: the northern point of convergence has been shifted onto Asia to overcome the singularity at the North Pole (Madec and Imbard 1996). Its space resolution is roughly equivalent to a geographical mesh of 2 by 1.5° (with a meridional resolution of 0.5°, near the equator). Thirty-one vertical levels are used with 10 levels in the top 100 m. The model time step is 1H40 mn. Horizontal diffusion is harmonic with an eddy coefficients of $2.10^3 \, \text{m}^2 \, \text{s}^{-1}$ for temperature and salinity and $4.10^4 \, \text{m}^2 \, \text{s}^{-1}$ for momentum. The eddy viscosity coefficient is reduced in the tropics to reach $2.10^3 \, \text{m}^2 \, \text{s}^{-1}$ at the equator. Vertical eddy diffusivity and viscosity coefficients are computed from a 1.5 turbulent closure scheme (Blanke and Delecluse 1993) which allows an explicit formulation of the mixed layer as well as minimum diffusion in the thermocline. The solar radiation is allowed to penetrate in the top meters of the ocean (Blanke and Delecluse 1993). Zero fluxes of heat and salt and no-slip conditions are applied at solid boundaries. The model does not include a sea-ice component but a simple parametrization that only involves a test on the sea surface temperature. If the ocean surface temperature becomes less than the freezing temperature then ice is present, a constant heat flux is applied to the ocean ($-2 \, \text{Wm}^{-2}$ in the Arctic Ocean and $-4 \, \text{Wm}^{-2}$ in the Antarctic Ocean) and the atmosphere GCM computes its own surface heat flux. This crude parametrization is not aimed towards modelling realistic sea-ice physics (for instance, heat and fresh water conservation is not ensured) and is inherited from early uncoupled ocean GCM simulations where the surface restoring terms were actually defining the sea-ice extension.

2.3 Experimental design

The ARPEGE and OPA models are coupled through the OASIS coupler developed at CERFACS (Terray 1994; Terray et al. 1995) which ensures the time synchronization between the two GCMs and does the spatial

interpolations from one grid to another. Daily mean sea surface temperature (SST) and sea ice extent (SIE) are given to the atmosphere GCM and daily mean surface fluxes of heat, momentum and fresh water are given to the ocean GCM. The coastlines of the two models do not match exactly and this slightly affects the transfer of the coupling fields in an integral sense. To avoid the spread of these local systematic errors, no attempt was made to ensure a global conservation of the fluxes after the interpolation. Moreover, the river flows diagnosed by the atmosphere GCM are not passed on to the ocean.

The atmospheric initial state is on January 1 of year 10 of an uncoupled integration of ARPEGE-T21 (AMIP run) forced by observed SST over the 1979–1988 period (Reynolds 1988). The initial ocean state is obtained as follows. The integration starts with January Levitus (1982) and is pursued over 10 years with an interior relaxation to monthly mean temperature and seasonal mean salinity of Levitus (1982) with a relaxation time scale of 50 days in the upper 800 m and 1 year in the deep ocean. The model is forced by monthly varying climatological wind stress (Hellerman and Rosenstein 1983), heat and fresh water fluxes (Esbensen and Kushnir 1981; Oberhuber 1988) plus a 12 day relaxation towards surface time varying temperature and salinity data of Levitus (Madec and Imbard 1996). After this *dynamic* spin-up, the thermodynamic structure remains quite close to the one of Levitus so that a comparison to the initial state will in fact be a comparison to the Levitus atlas.

From this initial state, we integrate the coupled model for 50 years (thereafter experiment **CE**). In parallel, an uncoupled ocean control experiment is performed, which is a continuation of the spin-up integration, but with no more internal restoring terms. This 50-year simulation is used as the ocean reference for the coupled simulation and is thereafter called **OR**. The atmospheric reference (thereafter **AR**) is issued from the 10 year AMIP run already described.

3 Climatology of the coupled simulation

The climatology of the coupled model is defined using the last 10 years of the simulation (years 41–50). The mean seasonal cycle is defined in terms of averages for each calendar month over the same period. Most of the drift in the atmosphere and the upper ocean occurred in the first 15 years of the simulation so that the largest features of the mean state and seasonal cycle analyzed here have been stable for the last 35 years of the run.

3.1 Air-sea interface and global energy budget

The air-sea interface is certainly the most critical region of a coupled model. In particular, the time evolution of the SST provides a good indicator of the model behavior. The annual and zonal mean SST, plotted as a function of latitude, is presented in Fig. 1. After an initial warming, the tropical SSTs remain stable for the last 40 years of the simulation. The mid-latitudes are stabilized in two years. The high latitudes response is antisymmetric with respect to the equator. A cooling occurs in the Arctic Ocean while the Antarctic regions warm up, leading to an almost complete sea-ice melt after 25 years. More generally, after the short 2-year adjustment phase of the ocean-atmosphere system, the time scales of the remaining drifts appear associated to ocean time scales rather than to atmosphere ones. Besides these "physical" time scales, a second quality of the model is the stability of the mean meridional distribution of SST. This equilibrium is well maintained for the last decades of the simulation and for most of the ocean surface north of 60 °S. This is all the more satisfactory as no flux corrections are applied at the air-sea interface. As expected from the SST evolution (Fig. 1), the net heat flux entering the ocean is in good agreement with the climatology for most latitudes (Fig. 2a). In the tropics the zonal heat flux structure of **CE** is shifted
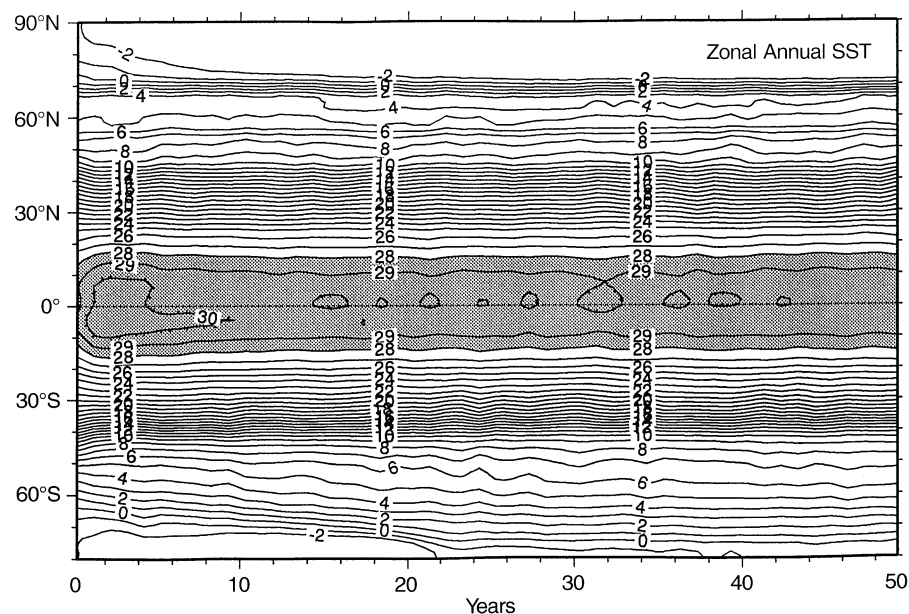

Fig. 1. Latitude-time diagram of the zonally averaged annual SST over the 50 simulated years. Values greater than 28 °C are *shaded* and contour interval is 1 °C
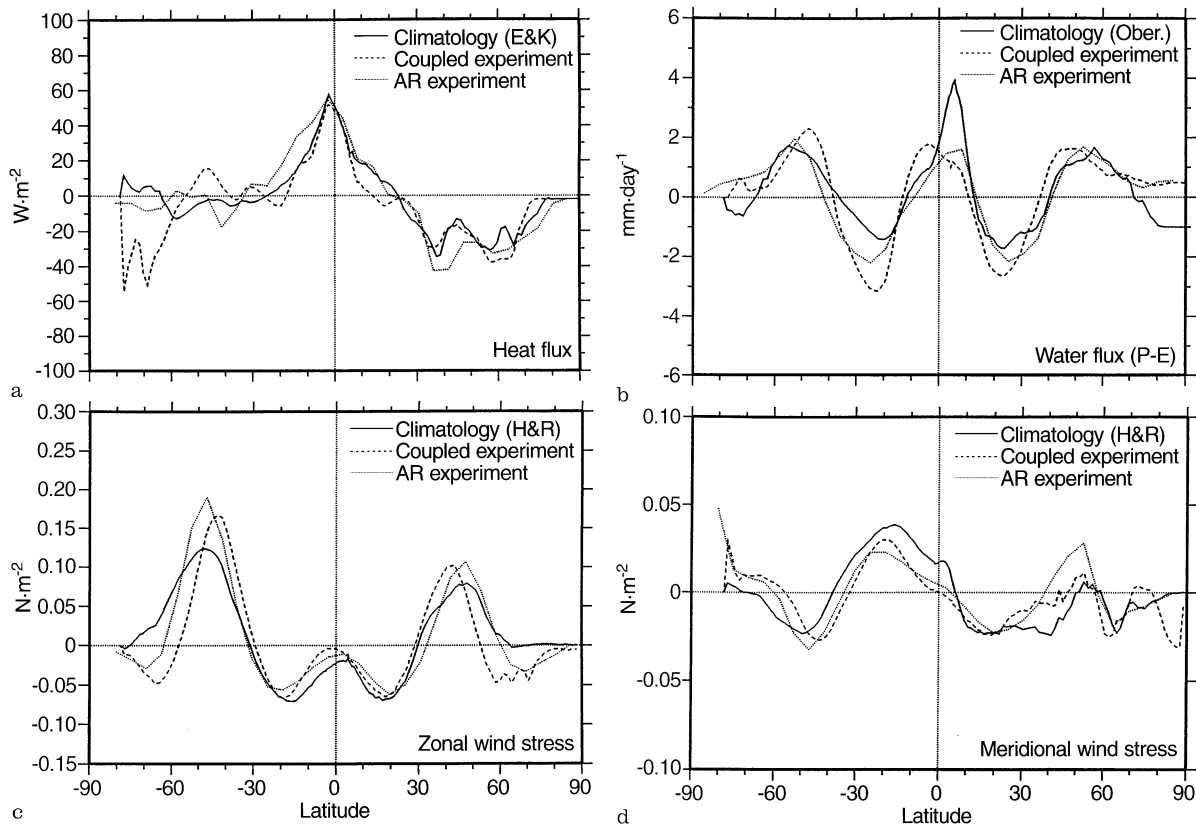
Fig. 2a–d. Zonal-mean surface ocean fluxes. Annual mean for climatology used to drive **OR**, years 41–50 average for coupled experiment **CE**, 10-y (AMIP) average for **AR**. **a** Heat flux, **b** water flux $(P - E)$, **c** zonal wind stress and **d** meridional wind stress

equatorwards when compared to that of **AR**. The net downward fresh water flux $(P - E)$ does not match the climatology as closely (Fig. 2b). The precipitation along the inter-tropical convergence zone (ITCZ) (5 °N) is underestimated and there is too much evaporation in the sub-tropics. In the tropics, the zonal wind stress is made symmetrical with respect to the equator (Fig. 2c). The mid-latitude westerlies are stronger than observed in both hemispheres (mainly due to a winter over-intensification) while their maxima is shifted equatorwards in **CE**. The trade winds near the equator are weakened throughout the year (in both Pacific and Atlantic oceans), while their tropical maximum (near 20 °N and 20 °S) is closer to observations than in **AR**. At the equator the weak northward meridional wind stress component present in **AR** becomes zero in the **CE** (Fig. 2d).

A global energy budget computed from the 10-year climatology of the coupled system is presented in Fig. 3. Through the top of the atmosphere (TOA), the net heat flux, defined as the difference between the incoming short-wave radiation flux $(+240.94 \ \mathrm{Wm}^{-2})$ and the outgoing longwave radiation (OLR) flux $(-240.82 \ \mathrm{Wm}^{-2})$, is very close to zero $(+0.12 \ \mathrm{Wm}^{-2})$. Between the different components of the system, the net heat flux is also small, except for the ice/atmosphere interface where it exceeds $20 \ \mathrm{Wm}^{-2}$. This important sea-ice heat loss to the atmosphere is imputable to the sea-ice model which does not conserve heat. A small systematic error of $1.0 \ \mathrm{Wm}^{-2}$
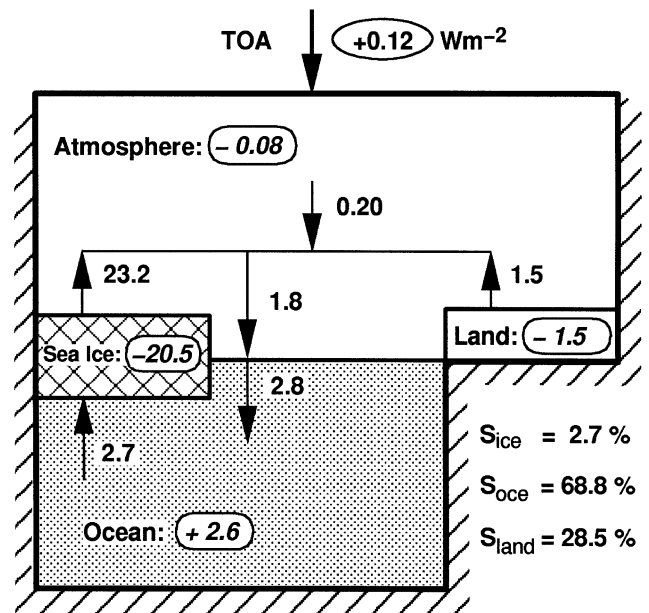

Fig. 3. Global energy budget of the coupled simulation. Annual mean from years 41–50. Units are Wm^{-2}. The interface budgets are given as *fluxes. Circled numbers* indicate storage. For integral calculations, the respective percentages of ice, ocean and land surfaces are added

(which represents a few per cent of the local heat flux) appears between the atmosphere and the ocean, due to the difference in the model coastlines. The small land-to-atmosphere heat flux (1.5 Wm^{-2}) results from the deep soil temperature restoration present in the two-layer soil scheme of the atmosphere GCM. All these internal heat sources are the main contributors to the ocean heat storage ($+2.6$ Wm^{-2}) which corresponds to a moderate global temperature drift of $+0.4\,°C$ per century and stress the need for a globally consistent modelling of the climate system.

The ocean, atmosphere and total meridional heat transports for **CE**, **OR** and **AR** are compared to the estimates of Trenberth and Solomon (1994) in Fig. 4. In both **CE** and **AR**, the total transport T_{A+O} is close to observational estimates, but without any correction for **CE**. Using the net ocean heat flux diagnosed by the atmosphere GCM, T_{A+O} can be split into T_{Oi}, the *indirect* northward ocean transport, and T_{Ai}, the *indirect* northward atmospheric transport. T_{Ai} is within the observation error bars in **AR** but this is no longer true for **CE** as T_{Ai} increased in the sub-tropics and in the northern mid-latitudes. In the ocean GCM, we are also able to integrate the *direct* ocean transport T_O. As expected, both T_{Oi} and T_O for the

coupled and uncoupled experiments are poleward at most latitudes (Fig. 4a,b). Interestingly, in the Northern Hemisphere (NH), T_{Oi} and T_O (which, in uncoupled mode, characterize the response of each GCM to climatological forcing) join each other close to the observed estimates of Trenberth and Solomon (1994) when the GCMs are coupled. The differences between T_{Oi} and T_O in **CE** result from the slight heat transfer misfits described in Fig. 3. For most latitudes, **OR** poleward heat transport T_O tends to be lower than the estimates of Trenberth and Solomon (1994). In **CE** this deficiency is increased in the south (equatorward of $40\,°S$) while T_O is closer to observations in the NH. The seasonal cycle of T_O is marked in the tropics (Fig. 5) where the heat transport is associated with the Ekman circulation (Oort and Vonder Haar 1976; Washington and Meehl 1989). Compared to **OR**, the northward tropical transport is increased during boreal winter and lasts longer, until May instead of until April at the equator. The maximum increase (2 *PW*) is located south of the equator. At the end of the austral winter (September–October), the southward heat transport is increased by 1 PW from $5\,°N$ to $15\,°S$.

Overall, the coupled model exhibits a balanced energy budget with realistic northward heat transports in both
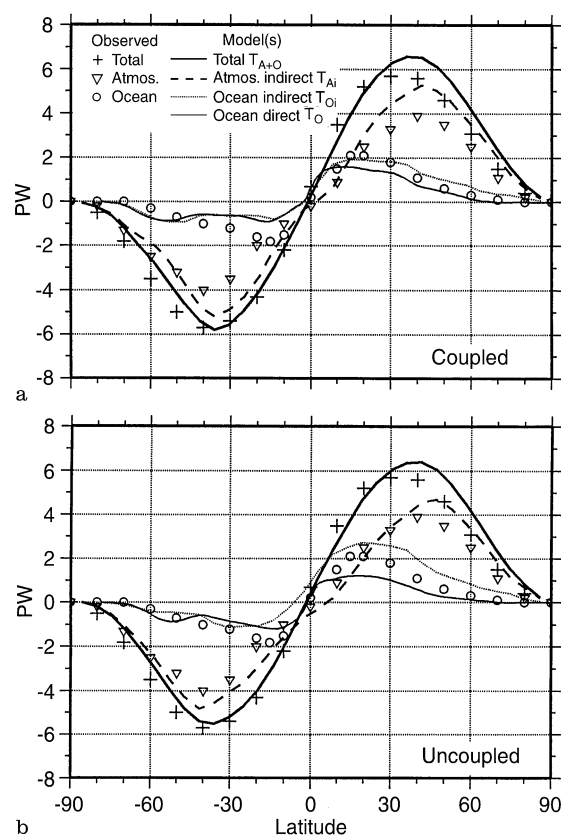

Fig. 4a, b. Northward heat transport in the ocean and in the atmosphere (PW). **a** Coupled simulation **CE**, **b** uncoupled simulations **AR** and **OR**. Symbols are observed estimates from Trenberth and Solomon (1994). As **AR** has a larger imbalance at the TOA ($+2$ Wm^{-2}), its associated northward transports are corrected assuming a constant error per surface unit
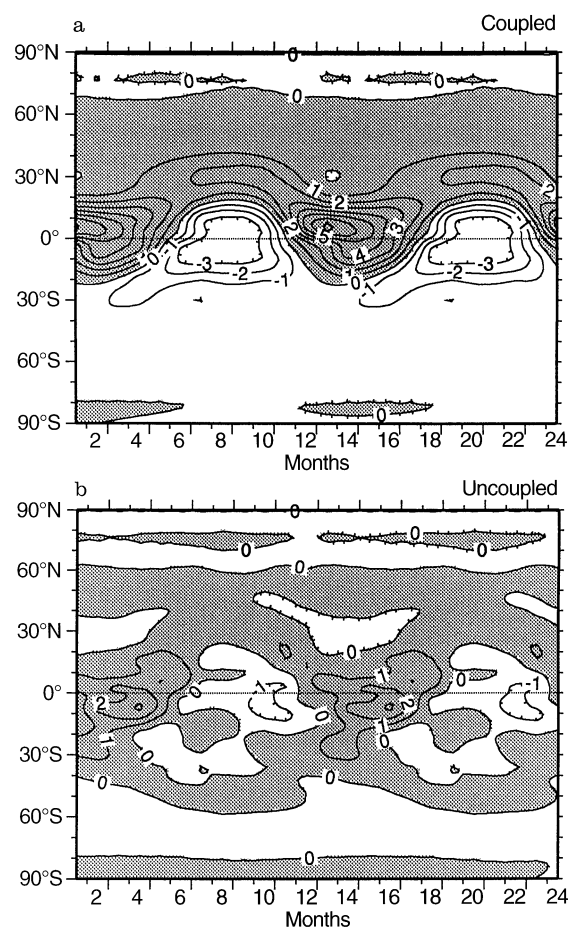
Fig. 5a, b. Latitude-time diagram of the seasonal cycle of the ocean northward heat transport T_O (reproduced twice). **a** Coupled experiment and **b** difference with **OR** uncoupled experiment. Contour interval is 1 PW and positive values are *shaded*
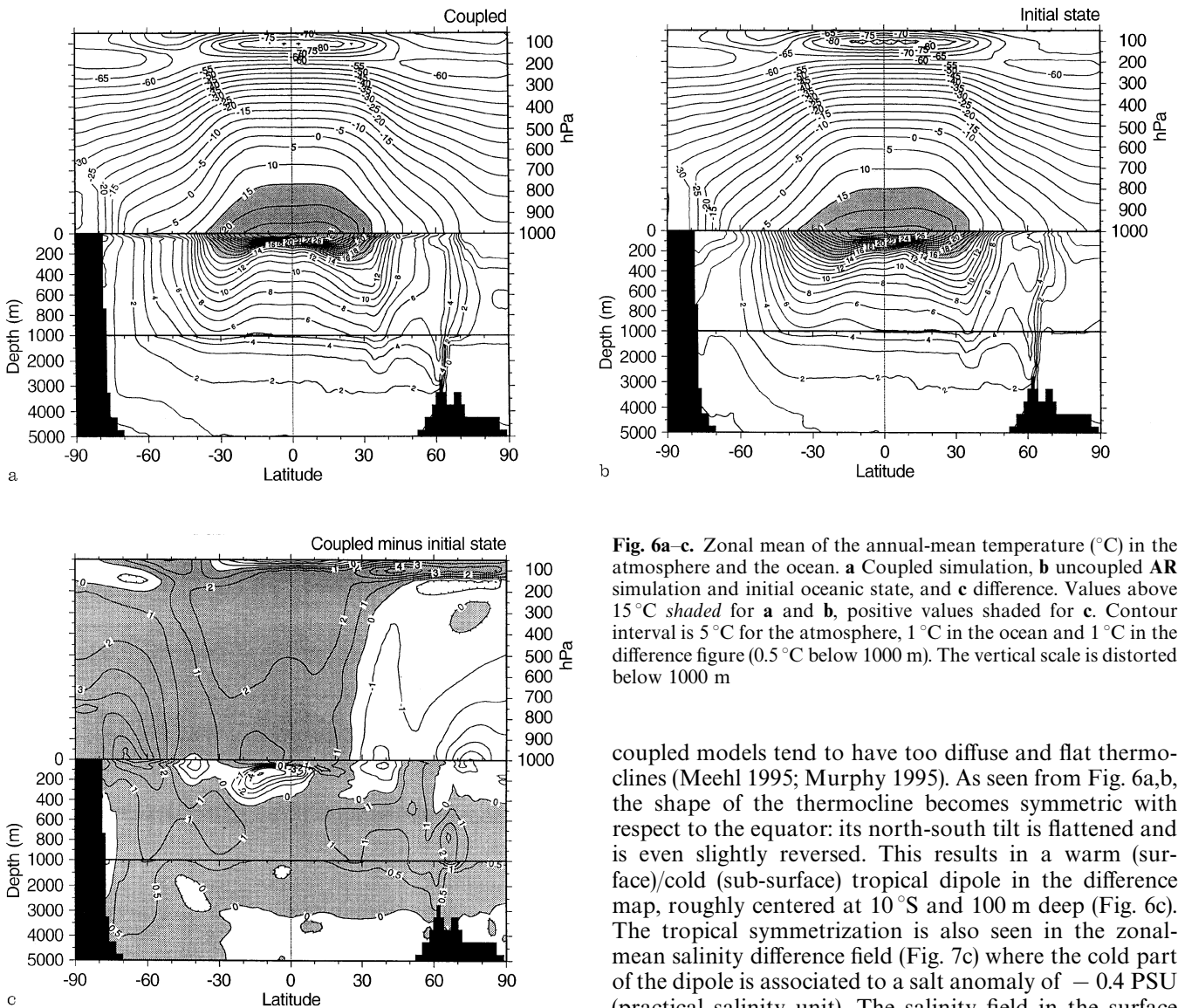
Fig. 6a–c. Zonal mean of the annual-mean temperature (°C) in the atmosphere and the ocean. **a** Coupled simulation, **b** uncoupled **AR** simulation and initial oceanic state, and **c** difference. Values above 15 °C *shaded* for **a** and **b**, positive values shaded for **c**. Contour interval is 5 °C for the atmosphere, 1 °C in the ocean and 1 °C in the difference figure (0.5 °C below 1000 m). The vertical scale is distorted below 1000 m

mediums. The northward ocean heat transport is increased when the ocean GCM is coupled, mostly due to a stronger Ekman transport in boreal winter.

3.2 Simulated ocean climatology

3.2.1 Thermohaline structure The zonal-mean temperature and salinity for **CE**, the initial state and their difference is shown in Figs. 6 and 7. In the tropics, the thermocline of the initial state is tight and shows a marked 'W' structure (Fig. 6b). This shape is well maintained all along **OR** and is a consequence of the vertical diffusion scheme used in the ocean GCM. The small vertical diffusion coefficient provided by the 1.5 turbulent closure scheme in the thermocline (less than 0.1 $cm^2 s^{-1}$) maintains the sharp gradient associated to the tropical thermocline. In coupled mode, these qualities are also present (Fig. 6a). This is an encouraging feature as many ocean-atmosphere

coupled models tend to have too diffuse and flat thermoclines (Meehl 1995; Murphy 1995). As seen from Fig. 6a,b, the shape of the thermocline becomes symmetric with respect to the equator: its north-south tilt is flattened and is even slightly reversed. This results in a warm (surface)/cold (sub-surface) tropical dipole in the difference map, roughly centered at 10 °S and 100 m deep (Fig. 6c). The tropical symmetrization is also seen in the zonal-mean salinity difference field (Fig. 7c) where the cold part of the dipole is associated to a salt anomaly of − 0.4 PSU (practical salinity unit). The salinity field in the surface layers (down to 200 m) follows the ITCZ extension to the south (Fig. 2b) and the associated salinity minima moves from 10 °N to 10 °S (Fig. 7). In the sub-tropics (20–30 °N and 20–30 °S), the increased evaporation seen in Fig. 2b leads to increased salinity at the surface, a characteristic which is then entrained inside the ocean equatorward of 30 °N and 30 °S (Fig. 7c). The southern penetration is partly offset by the sub-surface fresh patch already discussed. The intermediate water characteristics are modified (warmer and saltier) from their surface formation regions (∼ 60 °N and ∼ 60 °S) and equatorward down to 1000 m (Figs. 6 and 7).

The annual-mean SST distributions became quite zonal in the coupled model (Fig. 8). Besides the austral ocean (where no sea-ice is left all year round, except in the Weddell Sea), the most striking temperature differences occur in the eastern boundary region of tropical basins where differences greater than 5 °C can be found. These warmer-than-observed tropical SSTs are reminiscent of other coupled models (Gates et al. 1985; Meehl 1990; Terray et al. 1995). In the equatorial Pacific, the whole trade winds/eastern upwelling/thermocline slope system is
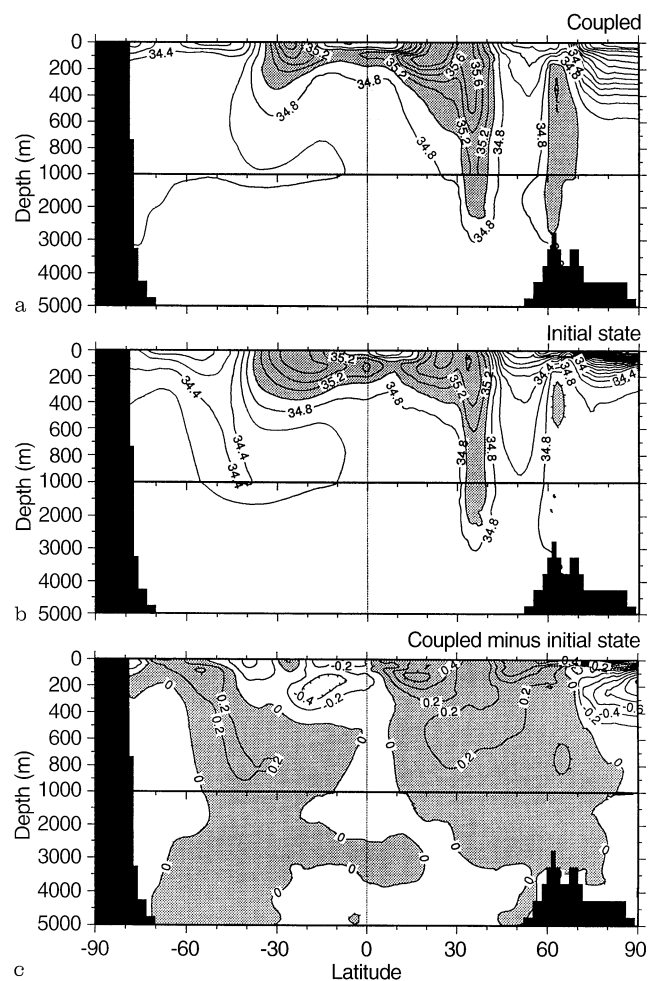
Fig. 7a–c. Zonal mean of the annual-mean salinity (PSU) in the ocean. **a** Coupled simulation, **b** initial oceanic state and **c** difference. Values above 35 PSU *shaded* for **a** and **b**, positive values *shaded* for **c**. Contour interval is 0.2 PSU. The vertical scale is distorted below 1000 m

Fig. 8a–c. Sea surface temperature (°C). **a** Coupled simulation, **b** initial state and **c** difference. Values above 26 °C *shaded* for **a** and **b**, positive values *shaded* for **c**. Contour interval is 1 °C

relaxed within a few months after the start of the coupled simulation. The trade winds collapse (Fig. 2c) is associated to a weakened eastern upwelling which further increases the warming of the SST in the eastern equatorial Pacific. The zonal SST gradient consequently weakens and so do the trade winds. This strong coupled mechanism is similar to the one invoked during an El Niño event and what triggers it is still unclear. Whatever the reason, the model, unlike reality, does not recover from this warm state. This permanent warm tropical state leads to a nearly flat thermocline along the equator (Fig. 9a), while the uncoupled model simulates a more realistic equatorial thermocline (Fig. 9b). Associated with the thermocline flattening, the warm water pool initially located in the Indonesian area now occupies most of the tropical Pacific ocean (Fig. 8a). A similar shift is seen in the tropical Atlantic ocean. The warm SST patches off the coasts of California, Peru and Namibia (Fig. 8c), also present in most coupled models, are due to an excess of solar radiation, generally associated with the lack of ability of atmosphere GCMs to
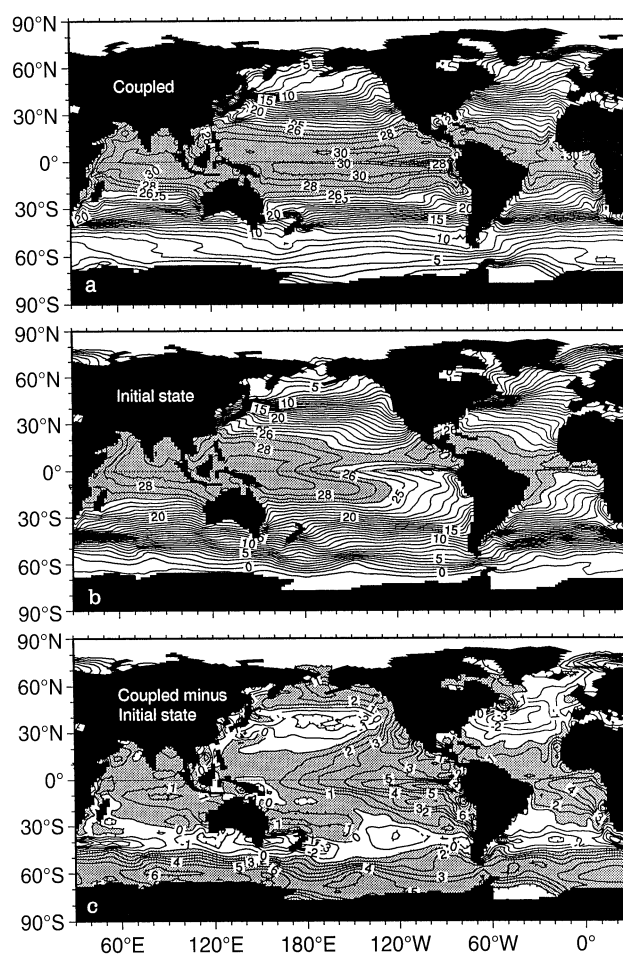
generate marine strato-cumulus clouds in these anticyclonic regions (Meehl 1995; Terray, personal communication 1996; Ma et al. 1996).

The seasonal variation of the ocean mixed layer affects the seasonal dependence of the simulated surface characteristics and is also an important determinant of the ability of the ocean to sequester heat from the atmosphere in an annual-mean sense. The main zonal-mean ocean mixed-layer depth difference between **CE** and **OR** are found in the extra-tropical regions (Fig. 10). An increase of the winter zonal wind stress over the northern Pacific (not shown) led to colder and slightly saltier surface waters, and hence spurious deep convection in the north Pacific (down to 400 m at 55 °N instead of 50 m in **OR**). This results in the deepening of the winter mixed layer between 30 °N and 50 °N (Fig. 10). Further north, the difference is due to the Atlantic where the North Atlantic Deep Water (NADW) formation is maintained in **CE** while it tends to collapse in **OR**. In the SH, the mixed-layer depth of **OR** reaches 375 m at 60 °S during September, but it is less than 100 m deep further south, as the sea-ice cover prevents strong air-sea exchanges. An increase of the salinity of the surface layers occurred along the Antarctica coast (possible causes are discussed in part 4), as seen from 50 °S to
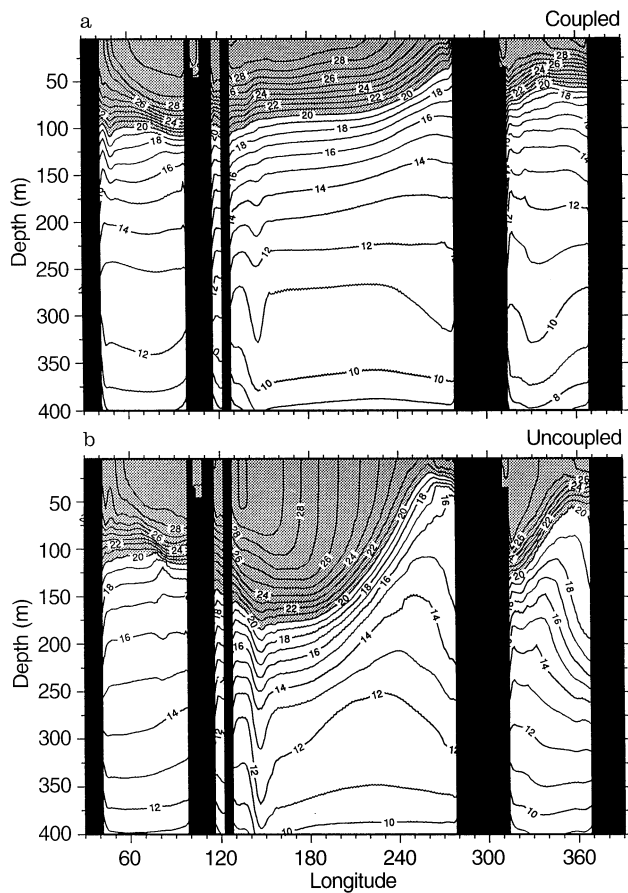
Fig. 9a, b. Equatorial section of temperature (°C). **a** Coupled simulation and **b** uncoupled **OR** simulation. Values above 20 °C *shaded*. The contour interval is 1 °C
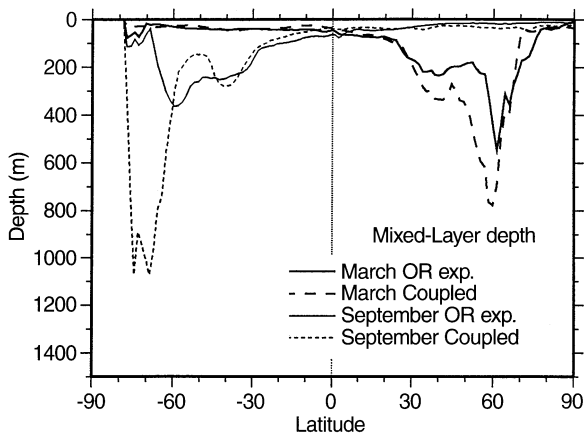

Fig. 10. Mixed-layer depth in March and September for coupled (*dashed curves*) and uncoupled **OR** (*solid curves*) simulations. diagnosed from the vertical mixing coefficient (or *turbocline* depth)

Fig. 11a–c. Meridional stream function in the ocean in Sv (1 Sv = 10^6 m^3 s^{-1}). **a** Coupled simulation, **b** uncoupled **OR** simulation and **c** difference. Positive values *shaded*. Contour interval is 5 Sv

70 °S in Fig. 7c. During winter cooling, this results in surface destabilization (hence convection) before the freezing point can be reached. As the ocean stability at 60–70 °S is weak, this results in the huge increase of the mixed-layer depth at 70 °S during austral winter (Fig. 10).

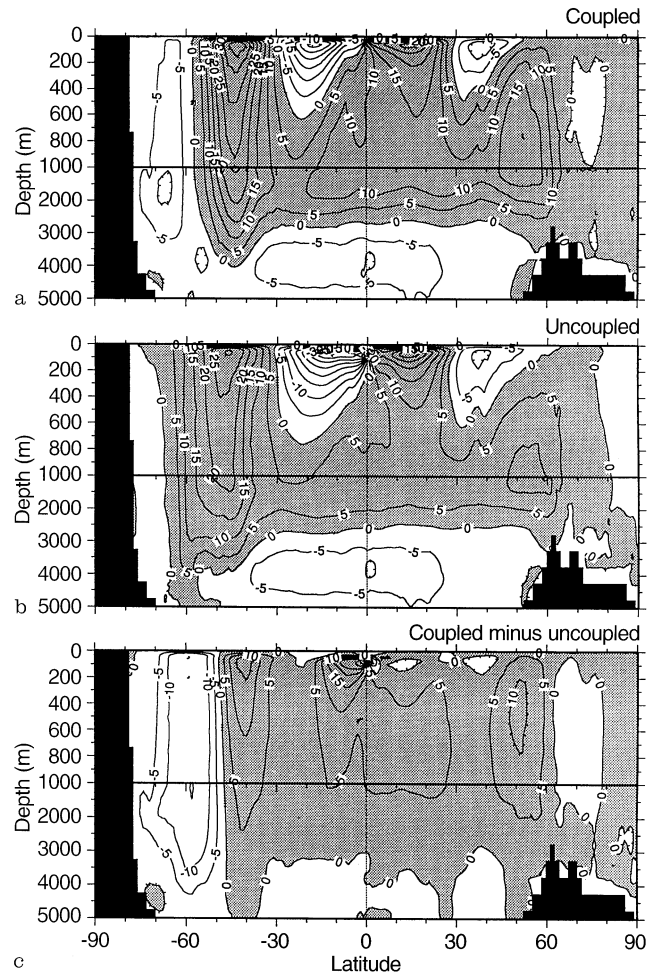This increased winter convection (down to 1000 m in zonal average) is seen in Fig. 6a where the isotherms become quite vertical around 70 °S. It is also associated with a spurious warming of the deep southern ocean (Fig. 6c, below 1000 m and poleward of 50 °S). In summer the temperature re-stratification takes place and no more convection occurs.

3.2.2 Ocean circulation The global ocean meridional stream function shows that the overall circulation in **CE** is well maintained both near the surface and in the deep ocean (Fig. 11). In the south, the wind-driven Deacon cell (40 °S–60 °S) is stronger than in **OR** (+15 Sv, 1 Sv = 10^6 m^{3}s^{-1}) and is shifted northward by about 5 ° in response to stronger westerlies (Fig. 2c). Following the trade wind weakening, the equatorial upwelling is reduced by more than 30 Sv (Fig. 11c). Consequently, the tropical Ekman cells are weakened, especially in the south where differences up to 20 Sv occur between 10 °S and 20 °S. In the northern mid-latitudes, a 10 Sv difference appears at 50 °N and 500 m deep. The Atlantic sector is responsible for half of this difference as the
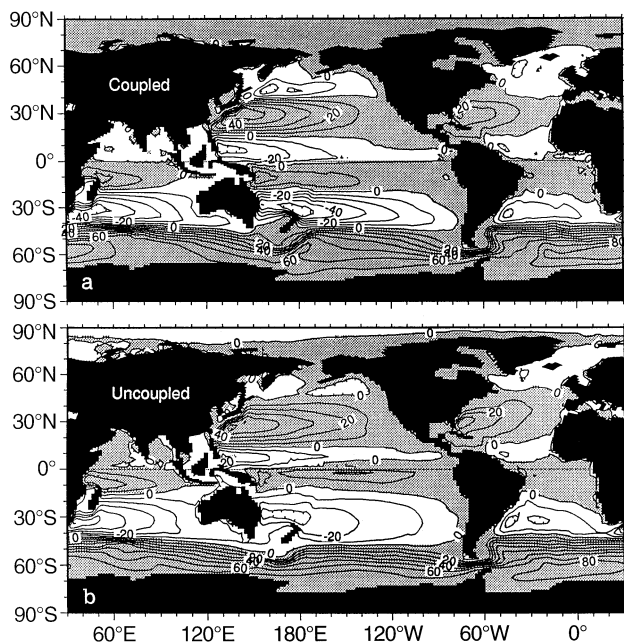
Fig. 12a–b. Barotropic stream function (Sv). **a** Coupled simulation, **b** uncoupled **OR** simulation. Positive values *shaded*. Contour interval is 10 Sv

Fig. 13a–b. Meridional stream function in the atmosphere (10^9 kg.s^{-1}). **a** Coupled simulation, **b** uncoupled **AR** simulation. Positive values *shaded*. Contour interval is 10. 10^9 kg.s^{-1}

NADW formation is well maintained in coupled mode when compared to the initial state, while it weakens in **OR** due to a spin-down of the circulation. The remaining 5 Sv difference is due to the appearance of a spurious overturning cell in the North Pacific (centered at 55 °N) associated to the increased convection seen in Fig. 10. Poleward of 60 °S, a counter-clockwise overturning circulation cell (5–10 Sv) appears in coupled mode down to 3000 m (Fig. 11a). This cell is linked to the important deep convection that occurs during winter at these latitudes which was already discussed (Fig. 10).

The barotropic stream function (BSF) shown in Fig. 12 is the vertical integral of the ocean mass transport and is mainly associated to the distribution of the wind stress curl. In the NH, the **CE** and **OR** BSF are in good agreement, but for the Pacific subpolar and subtropical gyres which are intensified in **CE** due to the stronger boreal winter wind. In the Pacific and Atlantic oceans, the tropical circulation becomes symmetric with respect to the equator. In the southern mid-latitudes the differences result both from the northern shift and the strengthening of the zonal wind that occurred in this region. The transport in the Drake Passage, close to 140 Sv in the initial state now averages 70 Sv for both **CE** and **OR**. This common barotropic response to two very different external forcings in the Antarctic circumpolar current or ACC (see Fig. 2) indicates that this drop of 70 Sv is due to the internal physics of the ocean. Indeed, the horizontal diffusion scheme in the ocean GCM is not able to maintain the tight meridional density gradient associated to the temperature and salinity fields in the top 1000 m of the ACC (Figs. 6 and 7) which most likely drives a part of the barotropic flow in the Drake Passage through the joint effect of baroclinicity and bathymetry (England 1993).
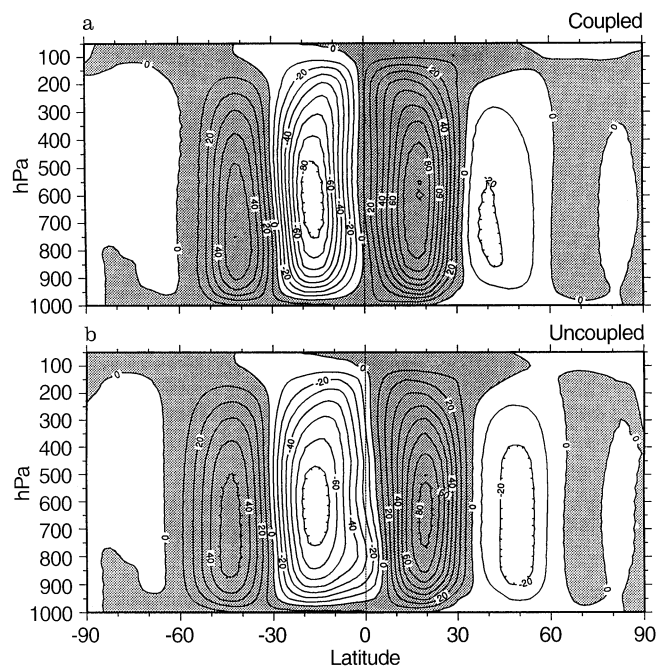
3.3 Simulated atmosphere climatology

In this section, we compare the atmospheric coupled model climatology (**CE**) to both **AR** and observations. The basic zonal-mean temperature distribution of **CE** is close to that of **AR** (Fig. 6). A common deficiency of uncoupled atmosphere GCMs, includes too cold polar stratosphere and non-polar troposphere (Boer et al. 1992; Déqué et al. 1994). This deficiency is significantly reduced in coupled mode (Fig. 6c). Following the increase of SST between 30 °S and 30 °N, the lower troposphere has warmed up, amplifying a tendency of the uncoupled atmosphere GCM (Déqué et al. 1994). This mostly results from changes in the atmospheric circulation (adiabatic heating) and is advected accordingly into the stratosphere (not shown). The cooling of the lower north-polar troposphere follows the surface cooling (extended ice cover) and is then diffused higher up. The warming of the south polar troposphere mostly results from an increased surface radiative heating linked to the lack of sea-ice in the 60 °S–70 °S latitude band and then also entrained in the upper troposphere by vertical diffusion, as also found by Royer et al. (1990). The atmospheric meridional stream function (Fig. 13) shows that the symmetrization already noted in the surface fields (Fig. 2c) also concerns the whole atmosphere. This feature is associated to a southern shift and to a strengthening of the northern Hadley cell in boreal winter. The ITCZ crosses the equator to the south during austral summer, a bias already slightly present in **AR** and amplified here. The too strong westerly winter and summer tropospheric jets deficiency noted by Déqué et al. (1994) in **AR** is amplified in **CE** (Fig. 14). This

intensification results from the tightening of the meridional temperature gradient which occurs in the troposphere around 30 °N and 40 °S (Fig. 6).

The distributions of the mean sea level pressure (MSLP) for **CE** and **AR** show an overall agreement in the tropical regions (Fig. 15). The main difference concerns the low

Fig. 14a–b. Zonal wind (ms^{-1}). **a** Coupled simulation, **b** uncoupled **AR** simulation. Positive values *shaded*. Contour interval is 5 ms^{-1}

pressure system associated with the Indonesian convection zone which moves to the east in **CE**. In boreal winter (DJF) the Icelandic and Aleutian lows extend to the southeast where the continental highs becomes very weak. The Icelandic low is less pronounced while the Aleutian low deepens by more than 10 hPa. The northeastward tilt of these low pressure systems is not properly simulated in coupled mode as also noted by Murphy (1995). The corresponding increase of pressure is due to the lower surface temperature that occur in the Arctic Ocean during winter. The Siberian high is too weak in DJF, and this is another common feature with Murphy's simulation. During JJA, the agreement in the NH between **CE** and **AR** is rather good, and the differences are mainly due to the equatorward shift of the high pressure systems of the North Atlantic and North Pacific oceans. The lack of sea-ice in the south and the change of the wind regime south of 45 °S (Fig. 2c) are associated with sizeable differences in the MSLP field all year long. These are added to the poor simulation of the Antarctic circumpolar lows already noted in uncoupled mode by Déqué et al. (1994).

In the tropics and during DJF, the zonal-mean precipitations of **CE** are higher than in the climatology but their meridional structure is in better agreement than those of **AR** (Fig. 16). During JJA, the ITCZ precipitation maximum at 10 °N is still underestimated although increased when compared to **AR**. Throughout the year, tropical precipitation is increased in **CE** as the SST is warmer there. The double ITCZ in JJA, a bias already present in **AR**, is enhanced in **CE**. At mid-latitudes, the precipitation is overestimated in both hemispheres and throughout the year. The coupled mode seems to accentuate this bias, especially in the winter hemisphere.
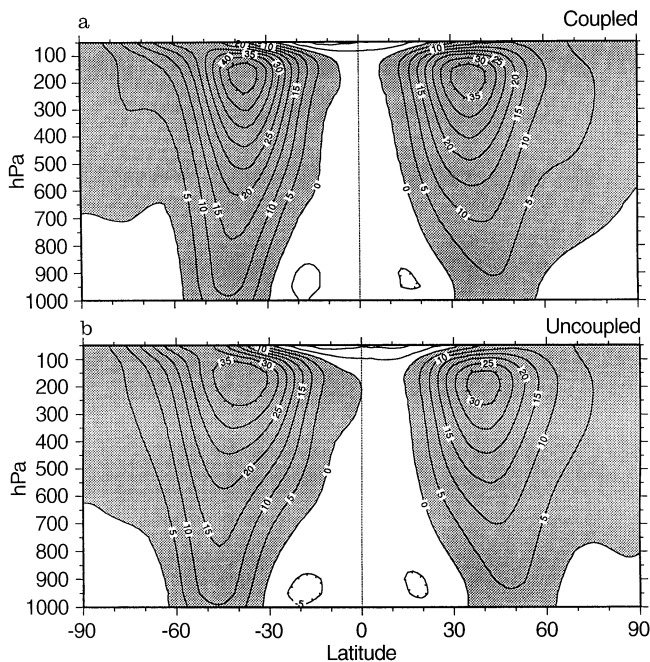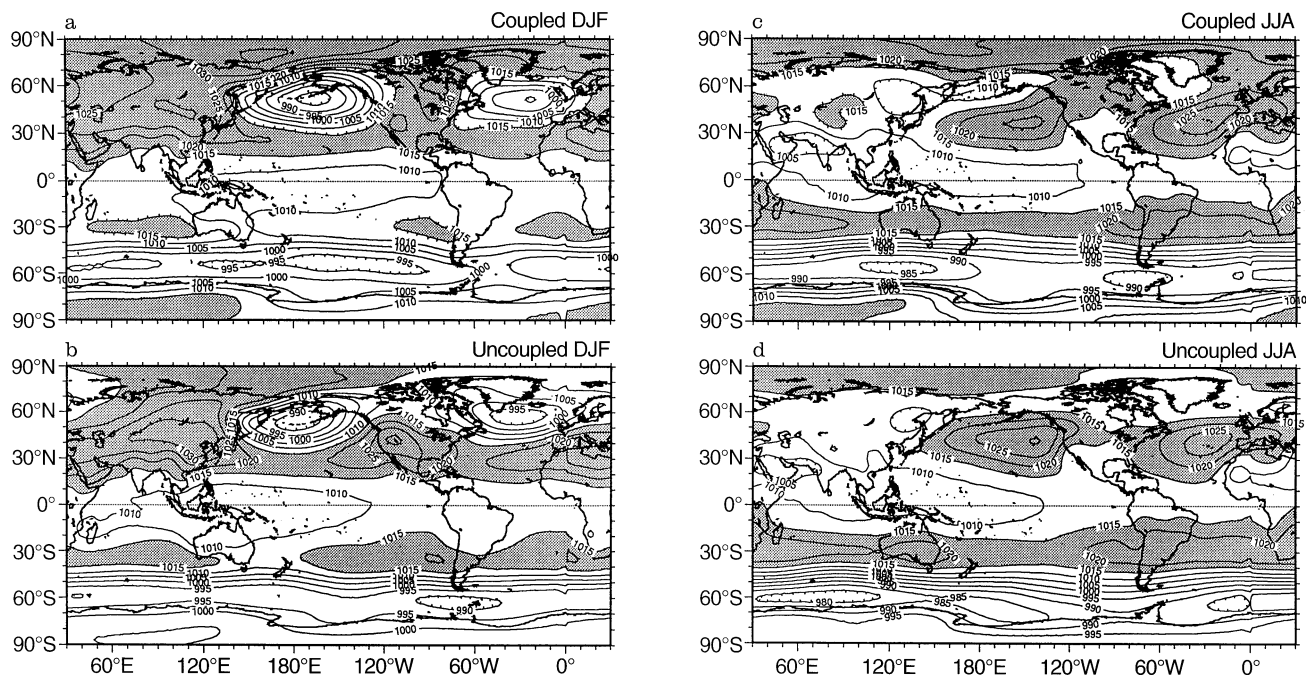

Fig. 15a–d. Mean sea level pressure (hPa). Coupled simulation and uncoupled **AR** simulation. **a, b**: DJF, **c, d**: JJA. Values above 1015 hPa *shaded*. Contour interval is 5 hPa
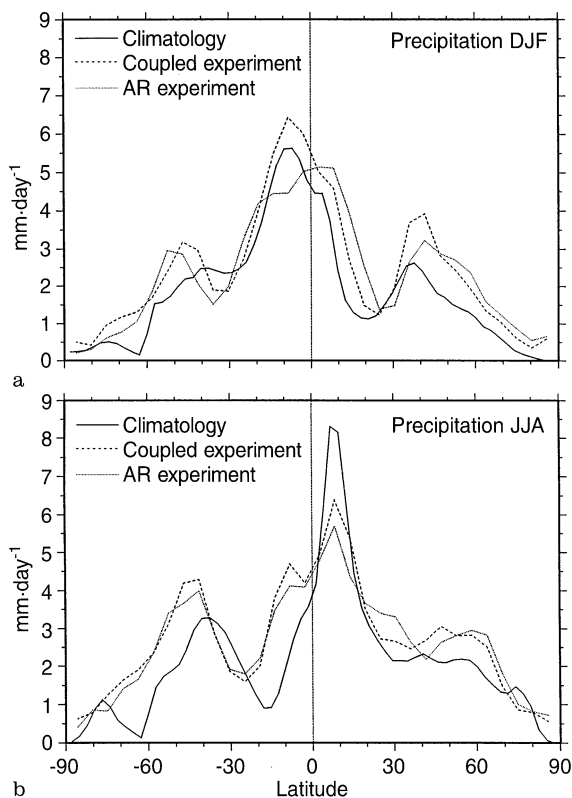
Fig. 16a, b. Zonal-mean total precipitation (land + sea) in mm.day^{-1}. Analysis of Xie and Arkin (1996) covering the period July 1987–June 1990 (*solid*), coupled simulation (*dahed*) and **AR** experiment (*dotted*). **a** DJF and **b** JJA
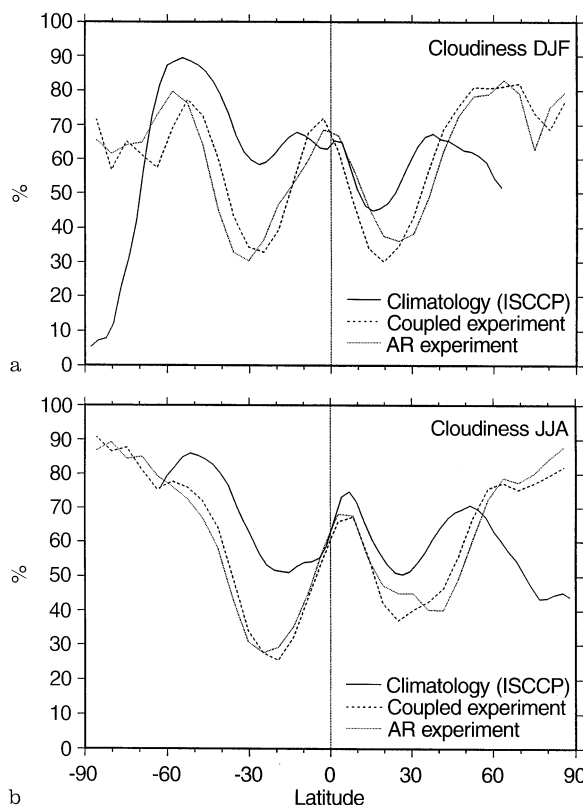

Fig. 17a, b. Zonal-mean cloudiness (%). ISCCP climatology (Rossow and Shiffer 1991) (*solid*), coupled simulation (*dashed*) and **AR** experiment (*dotted*). **a** DJF and **b** JJA

The lack of marine strato-cumulus over the eastern sub-tropical oceans has been identified in a number of atmosphere GCM (Meehl 1995; Ma et al. 1996) and both **CE** and **AR** lack between 20% to 30% of cloudiness outside the equatorial band when compared to observations (Fig. 17). Between 10 °N–30 °N, the reduced cloudiness in **CE** explains the too important evaporation in the *P–E* budget (Fig. 2b). The meridional distribution of outgoing longwave radiation (OLR) shows a rather good agreement with the Earth Radiation Budget Experiment (ERBE) data (Fig. 18). In the tropics, the atmosphere GCM tends to overestimate the OLR (in absolute value), an error amplified in **CE** where differences up to 20 Wm^{-2} are seen. This mostly results from a too diffuse convection in the tropics, which leads to convection clouds that are not high enough (their top is therefore warmer), hence increased OLR in absolute value. At 20 °N and 20 °S, the OLR is further increase following the decrease of cloudiness there (Fig. 17). The cloud radiative forcing (CRF) is defined as the difference between the net radiation at the top of the atmosphere with the given distribution of cloudiness and the corresponding clear sky net radiation. It measures the effect of the clouds in the earth radiative balance (Ramanathan et al. 1989; Wallace 1992; Gleckler et al. 1994). Its longwave component is associated with the *greenhouse effect* (warming of the atmospheric column) while its shortwave component is associated with the *albedo effect* of the clouds (cooling of the atmospheric
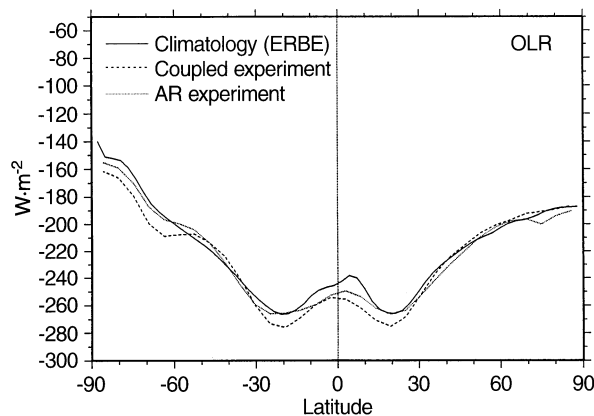

Fig. 18. Zonal-mean annual outgoing longwave radiation at TOA (OLR) in Wm^{-1}. ERBE climatology averaged over 1985–1988 (Barkstrom 1984) (*solid*), coupled simulation (*dashed*) and **AR** experiment (*dotted*)

column). The zonal-mean CRF of **CE**, **AR** and ERBE are given for DJF and JJA in Fig. 19. In the tropics, both **CE** and **AR** overestimate the cooling due to the CRF. This difference results from the underestimation of the longwave component of the CRF in that region: as the convection is too diffuse, the associated greenhouse effect is too weak. In the sub-tropics, the lack of low clouds reduces
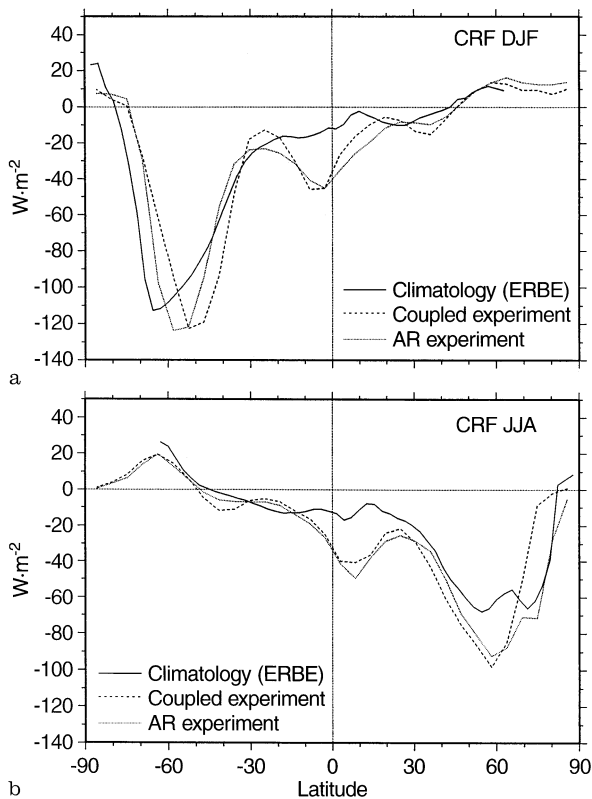
Fig. 19a, b. Zonal-mean cloud radiative forcing (CRF) in Wm^{-1}. ERBE climatology (*solid*), coupled simulation (*dashed*) and **AR** experiment (*dotted*). **a** DJF and **b** JJA

the cooling due to the albedo effect but, as the greenhouse effect is also reduced, the resulting total CRF remains close to observations.

4 Discussion

4.1 Tropics

The most striking feature of the tropical climate is the permanent warm mean state. The persistence of this warm state leads to most of the deficiencies noted in the climatology of the tropical regions and in particular in the Pacific basin. Associated with the weak equatorial tradewinds, the Indonesian convection zone extends eastwards in the tropical Pacific, leading to ENSO-like MSLP anomaly pattern with high pressure over Australasia and low pressure over the eastern Pacific (Fig. 15). The Indonesian convection activity moves to the center of the basin and is everywhere intensified due to the higher tropical SSTs. The zonalization and symmetrization of the atmospheric circulation and the SST further amplifies the convection difference south of the equator, between 180°E and 130°W (not shown). In the east of the basin, the north–south seasonal cycle of the ITCZ is amplified and its annual-mean position is now located south of the equator (Fig. 8a). The associated wind stress changes

(around 15 °S in Fig. 2c, d) implies a negative curl of the wind stress in this region and, as this is in the Southern Hemisphere, the associated Ekman pumping is now positive. This implies a 20 Sv MSF anomaly (Fig. 12c) and a shallower thermocline at 15 °S. As this process occurs in a strong vertical gradient region, it leads to the sharp tropical warm/cold dipole seen at 15 °S in Fig. 6c. The warmer-than-observed tropical SSTs, together with the associated deficiencies previously discussed, indicate that the coupled system has initially drifted away from the observed state before settling in the regime already described. However, the simulated thermocline is tight and close to the surface (Fig. 9) and the lack of cold water upwelling is thus more a result of the collapse of the equatorial trade winds than a deficiency of the ocean structure (as was invoked for several other coupled models, Meehl 1995).

The onset of this ENSO-like warm tropical mean state seems to be equatorial and involves the relaxation of the trade winds/eastern upwelling/thermocline slope system (see Sect. 3.2.1). Of course, what triggers it is a delicate question. The model's climatology shows an excess of local solar radiation associated with the lack of low-level marine strato-cumulus clouds in the eastern sub-tropics and this can contribute to warmer SSTs there. This effect is associated with the zonalization of the wind structure which implies a lack of northward wind in the east of the basin and consequently a reduced upwelling of cold waters off the coast of Peru. These two deficiencies can contribute in triggering the equatorial feedback loop described above but further analyses are needed for a firm conclusion. Neveretheless, in the TOGA coupled version of the OPA/ARPEGE-T42 coupled model, Terray et al. (1995) also observed warm and stable SSTs in the tropical Pacific associated with similar deficiencies in the atmospheric component. Their detailed analysis of the tropical coupling also suggests that these atmospheric deficiencies result in the spurious initial warming of the tropical SST. The present model has a coarser resolution, in particular in the atmosphere, and the tropical dynamic in the two fluids is consequently degraded in coupled mode. However the main responses are qualitatively the same, and this strongly suggests that similar tropical mechanisms are at play in both models. The stabilization of the tropical SSTs, which follows this warming phase, results both from the existence of an SST upper limit implied by the ocean-atmosphere feedbacks, and from the tight tropical thermocline which acts as a thermal barrier between the cold interior-ocean waters and the warm mixed-layer waters.

One might further wonder if a permanent ENSO-like mean state means no more ENSO-like interannual variability. The SST anomalies in Niño 3 region (Fig. 20) show that there is indeed such low frequency variability in the equatorial eastern Pacific (Pontaud 1996). Although its amplitude and phase do not appear unrealistic, we can nevertheless wonder if it corresponds to an ENSO-type variability : the mean state is very different and the Niño 3 anomaly analysis (best spatially suited for the observed mean state) is restrictive.

With a global ocean GCM, we can assess the role of the ocean in transporting energy away from the tropics. The ocean meridional heat transport T_O can be split

into components associated with overturning circulation, large-scale gyre circulation and lateral diffusion. The overturning component associated with the Ekman cells dominates in the tropics (Fig. 21). In coupled mode, the symmetrization of the circulation nullifies the northward heat transport at the equator. In parallel, the modified trade winds and the increase of temperature in the surface layers (Fig.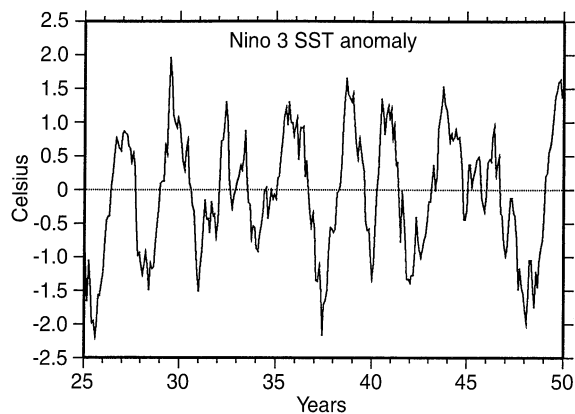 6c) leads to increased northward overturning heat transport in the whole tropics during boreal winter (maximum of $+2$ PW in Fig. 5b). Conversely, but to a lesser extent, the southward transport is enhanced during summer (minimum of -1 PW in Fig. 5b). In the northern tropics, this net increase enables the annual-mean T_O to compare well with observations (Fig. 4a) but not for the right reasons. In the south (between 15°S and the equator), this increased overturning component is partly compensated by an important decrease of the northward gyre component (Fig. 21d), mostly due to the zonal flattening of the thermocline. Nevertheless the annual-mean southward total transport in the southern tropics is still decreased by 0.5 PW down to 30°S (Fig. 21a).

4.2 Mid-latitudes

In the atmosphere, the most noticeable mid-latitude feature is the zonalization of the circulation. In both hemispheres, the whole atmospheric circulation is shifted equatorwards and is intensified, following the tightening of the SST meridional gradient implied by the warmer tropical SSTs and the colder mid-latitudes SSTs (Fig. 8c). Following this shift, the position of the front associated with western border currents has shifted equatorwards between **OR** and **CE**. In **OR**, the position of these currents is too far poleward when compared to the climatology and the
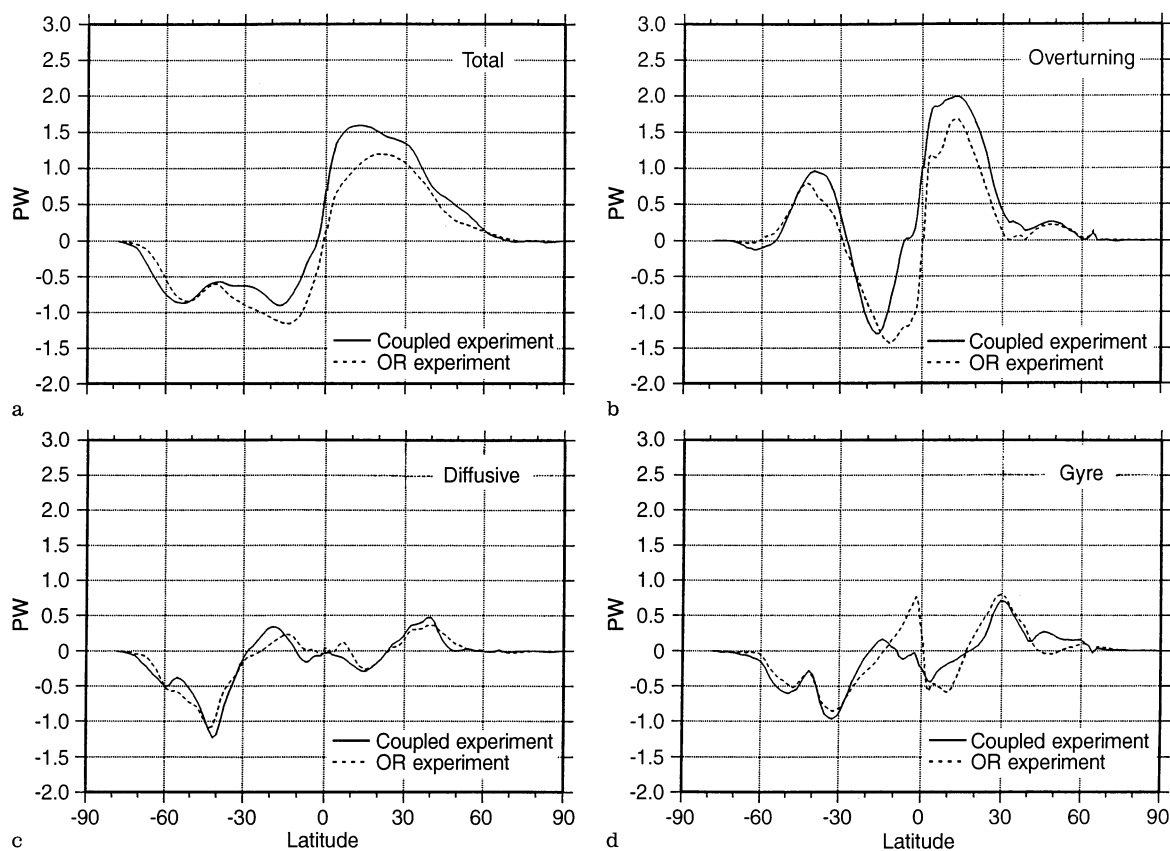

Fig. 20. Monthly SST anomaly in Niño 3 box for years 25–50 (°C)

Fig. 21a–d. Northward heat transport in the ocean (PW). Coupled simulation (*solid*) and uncoupled **OR** simulation (*dashed*). **a** Total transport (reproduced from Fig. 4), **b** overturning component, **c** diffusive component and **d** gyre component (as defined by Meehl et al. 1982)
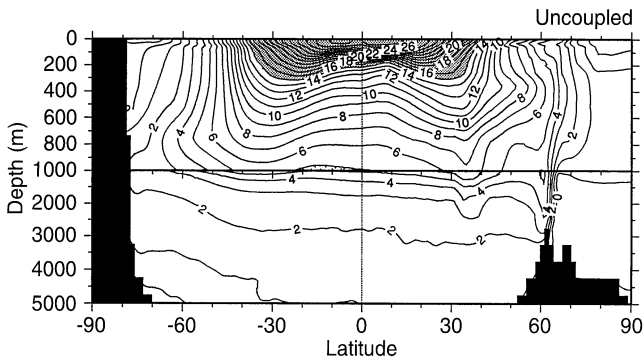
Fig. 22. Zonal mean of the annual-mean temperature (°C) of the uncoupled **OR** simulation. Values above 15 °C *shaded*. Contour interval is 1 °C (0.5 °C below 1000 m in **b**). The vertical scale is distored below 1000 m

Fig. 23. Time evolution of annual-mean areal sea-ice cover (10^7 km^2). Arctic (*solid*) and Antarctic (*dashed*)

surface feedback terms are quite important in these regions. In coupled mode, the ocean-atmosphere exchanges are consequently strongly reduced there but this is rather an improvement from the uncoupled mode. In the North Pacific, the deepened Aleutian low (Fig. 15) is consistent with a permanent ENSO-like mean climate.

In the SH, an important southward diffusive heat transport (1.2 PW at 45 °S) takes place across the ACC (Fig. 21c). As the northward overturning component (in the Deacon cell) and the southward gyre component more or less balance each other, the Southern Ocean is warmed by this spurious diffusive contribution. This spurious ocean process is also clearly visible in **OR** (50 °N, 500 m deep and 50 °S–70 °S, 800 m deep in Fig. 22) and is due to the horizontal diffusion scheme used in the ocean GCM, which erodes horizontal temperature and salinity gradients. The misrepresentation of the intermediate waters is also largely a result of this spurious enhanced horizontal diffusion and the intensity of the associated temperature and salinity modifications is associated with the initial strength of the horizontal gradients of temperature and salinity (Figs. 6 and 7). Furthermore, in **CE**, the surface feeding of the intermediate waters is blocked due to the increased buoyancy implied by the surface ocean warming (Fig. 6). The implementation of an isopycnal diffusion scheme in the ocean GCM is under way and should reduce this diffusive deficiency (Murphy 1995).

4.3 Sea-ice

Figure 23 shows the 50-y time evolution of annual mean areal sea-ice cover in the Antarctic and Arctic oceans. The most striking feature is the gradual melting of the Antarctic sea-ice, which falls to 20% of its initial surface after 25 years and is reminiscent of other coupled models (Washington and Meehl 1989; Murphy 1995). As seen previously, the ice cannot form in austral winter due to the high salinity of the surface waters in the simulated mean climate (convection occurs before freezing point can be reached). Several causes can be proposed but the conclusion requires the analysis of the initial phase of the
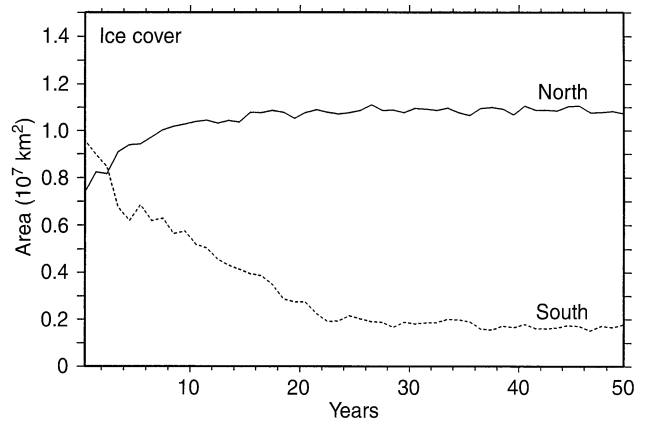
simulation, as the processes that increased the salinity there may not be active 30 or 40 y after. The first possible cause is linked to the sea-ice cycle itself: in the real world, ice forms near the coast (salt rejects), is advected by winds and melts away from it (fresh water release). None of these processes is modelled here and this can contribute to the gradual increase of surface salinity between 50 °S and 60 °S. Second, the spurious heat diffused across the ACC by the ocean GCM, in addition to too warm atmosphere heat fluxes, could have gradually pushed the ice limit south (as seems implied by Fig. 1), the (strong) winter wind mixing bringing the initial subsurface higher salinity water to the surface. Washington and Meehl (1989) invoke warming by horizontal diffusion in the ocean GCM to explain the melting of the sea-ice around Antarctica in their coupled model. Murphy (1995) relates this melting to the weak vertical stability of the Southern Ocean where small errors can have large effects. Indeed, in this coupled simulation which includes a thermodynamic/dynamic sea-ice model, surface flux correction terms and isopycnal diffusion in the ocean, the SH sea-ice also decreases to 20% of its initial coverage. It takes 50 years in this case to reach that value (against 25 for the present simulation) and this could be related to a smaller southward diffusive heat transport at 60 °S (0.6 PW against 1.2 PW). Whatever the main cause, it is clear that two kinds of processes interact non-linearly with the sea-ice seasonal cycle: *convective* which mostly depend on surface fluxes and have short time scales (seasonal up to a couple years) and *diffusive* which mostly involve ocean interior physics and have longer time scales (up to several decades). The time evolution of the Southern Hemisphere sea-ice coverage (Fig. 23 or Murphy's Fig. 22a) clearly exhibit both time scales. Consequently, and in the light of the other coupled model's results discussed, a more detailed sea-ice model is not likely to solve this southern sea-ice disappearance by itself. The Arctic Ocean is a Mediterranean-type sea and has a marked halocline. Consequently the processes at play in the south cannot be very active here. This explains why the sea-ice coverage is maintained in the Arctic Ocean. The increase seen in Fig. 23 is mostly due to gradual extension of sea-ice in summer in the Norwegian

Sea, associated with the weakening of the North Atlantic Drift (Fig. 12).

4.4 Sea surface salinity

This discussion can be summarized when looking at the sea surface salinity (SSS) field which is a good field for assessing the global performance of a coupled GCM. Unlike the SST, errors in this surface field cannot be compensated by direct coupled ocean-atmosphere feedbacks. Furthermore, the SSS integrates the $P–E$ field produced by the atmosphere GCM. Thanks to these two unique features, the signature of many coupled model's deficiencies can be found in the SSS distribution. To illustrate this, Fig. 24 presents the SSS field for **CE** and **OR**, the latter being close to the Levitus atlas due to the surface restoring term. First the zonalization of the field is striking, especially in the south. This results from the zonalization of the ascendence and subsidence zones which implied a zonalization of the precipitation and evaporation distributions. The excessive salinities in the

eastern sub-tropics (up to $+1.2$ PSU off the coasts of California and Chile) result from the large evaporation due to the excessive solar radiation implied by the lack of low clouds there and possibly from a weaker-than-observed upwelling of low-salinity sub-surface water there (Washington and Meehl 1989). The fresher patch centered in the south-tropical Pacific (as well as the one in the southwestern tropical Atlantic) (Fig. 24c) reveals that intense precipitation, thus atmospheric convective activity, now takes place there and shows the southern extention of the ITCZ. The high SSS around Antarctica (except in the Weddell Sea) was just discussed and, in the Arctic Ocean, the higher SSS are due to the erosion of the halocline which is also visible in Fig. 7. The lack of river runoff into the ocean is clearly seen at the mouth of the major rivers (Amazon, Ganges, Niger-Congo, Arctic rivers, …). This wealth of information obtained from the SSS field is importantly reduced in the uncoupled ocean GCM (because of the surface feedback terms) and is possible in coupled mode provided that no artificial flux correction techniques are applied at the air-sea interface.

5 Conclusion

The climatology of the OPA/ARPEGE-T21 global coupled model is assessed. The model reasonably simulates the basic features of the observed mean state and seasonal cycle of the ocean-atmosphere system. As no flux correction techniques are used, a first quality of the model is the good stability of the simulated air-sea interface which is maintained for several decades and for most of the ocean surface. The first contribution to this stability is the balanced radiation budget at the top of the atmosphere ($+0.12$ Wm^{-2}), already present in the uncoupled atmosphere GCM (Déqué et al. 1994), but to a lesser extent. In the tropical ocean, the simulated thermocline is tight, has a marked **W** meridional structure and realistically acts as a thermal barrier between the cold interior-ocean waters and the warm mixed-layer waters. These features are also presented in the uncoupled ocean GCM (Madec and Imbard 1996). In the present experiment, they contribute to the stability of the coupled system because, on one hand, they prevent the tropical SSTs from drifting to colder values (as seen for instance in other coupled models using no flux correction technique – Washington and Meehl 1989), and, on the other hand, they avoid a warming of the waters below the thermocline. Associated with this stability, the coupled model exhibits a balanced global energy budget and realistic annual-mean northward heat transports in both ocean and atmosphere showing that both components adjusted to each other. Furthermore, the model simulates a marked seasonal cycle at mid-latitudes consistent with available observations and the global ocean thermohaline circulation is well maintained.

Nevertheless, some systematic deficiencies are identified, including too warm tropical SSTs leading to a permanent ENSO-like mean state, a degraded seasonal cycle in the tropics, a zonalization and a symmetrization of the ocean-atmosphere circulation, a modified winter atmospheric circulation in the northern mid-latitudes and
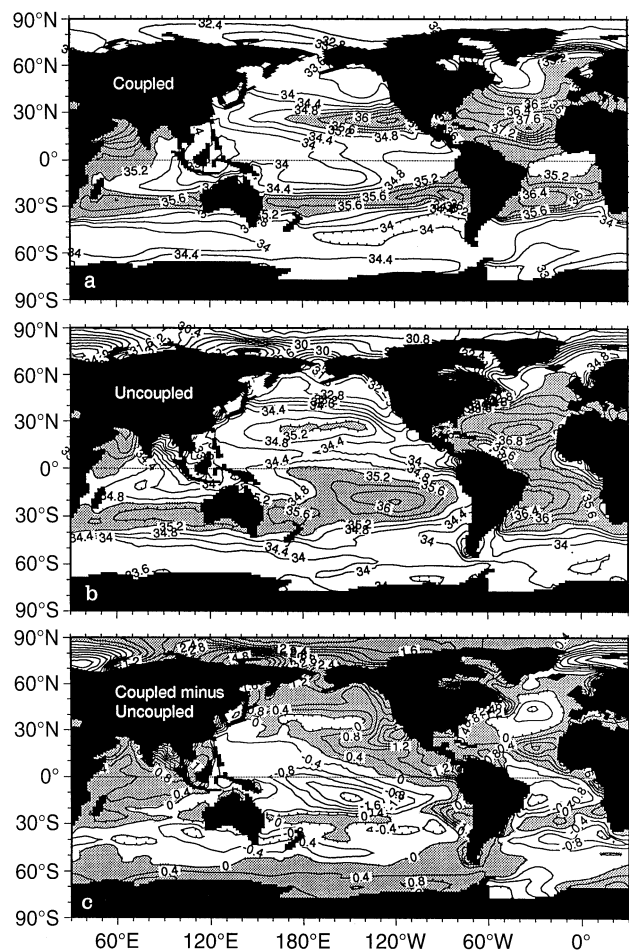

Fig. 24a–c. Sea surface salinity (PSU). **a** Coupled simulation, **b** uncoupled **OR** simulation and **c** difference. Values above 35.2 PSU *shaded* for **a** and **b**, positive values *shaded* for **c**. Contour interval is 0.4 PSU

a warming of the Southern Ocean associated with an almost complete melting of the Southern Hemisphere sea-ice. Most of these deficiencies are already present in the uncoupled reference simulations and are further amplified by the coupling. The zonalization and the tropical symmetrization with respect to the equator were already noticeable in the uncoupled atmosphere GCM. The lack of low clouds above the eastern part of the subtropical ocean basins is a common deficiency of atmosphere GCMs, also present in the model used here. It is due to the absence of a proper parametrization and illustrates the need for improvements in the physical parametrizations in the atmospheric marine boundary layer. These were initially developed in uncoupled mode and need to be revisited in the light of the coupled processes seen in the present simulation. In particular, the humidity and cloud distributions in the boundary layer must be simulated accurately. Their key role in the warm tropical bias observed here is likely and was also noted by other authors (Terray, personal communication 1996, Ma et al. 1996).

The mid-latitudes ocean deficiencies are shown to be both due to a larger-than-observed diffusive bias inherent to the ocean GCM physics and to an equatorward shift of the atmospheric circulation. In the southern high-latitudes, the stability of the no-sea-ice mean state is shown to be related to high salinity surface waters, preventing freezing before convection can occur. The processes that led to this high salinity mean state are still unclear although they probably involve both convection in response to modified atmospheric fluxes and spurious southward heat diffusion in the ocean GCM. As many other coupled GCM exhibit a similar drift, the simple sea-ice parametrization used here cannot be solely responsible for the modified sea-ice distribution, and the oceanic and atmospheric components most certainly have significant roles in this drift. Nevertheless a thermodynamic/dynamic sea-ice model is being developed and will be included in future coupled simulations.

Besides the deficiencies inherent to the uncoupled GCMs, some strong coupled processes appear and lead to unrealistic features that cannot be identified when the GCMs are driven by climatological boundary conditions. The warmer-than-observed tropical SSTs and the melting of the sea-ice in the Southern Hemisphere are likely to result from such coupled processes. These deficiencies are very interesting features as they emphasize physical processes at play within the coupled system which were poorly taken into account in the uncoupled GCMs. More work is needed to elucidate them within such complex GCMs. In particular, a careful analysis of the initial drift phase of the simulation has been undertaken and is likely to give some precise insights. Other studies conducted with different versions of the OPA-ARPEGE coupled model show that the warm bias together with the stability at the tropical air-sea interface, and the disappearance of the Southern Hemisphere sea-ice are persistent when the resolution is increased in both GCMs (Terray et al. 1995; Pontaud et al. 1995; Pontaud 1996; Delecluse and Levy, personal communication 1995). This suggests that the model is misrepresenting or even omitting some coupled mechanisms which results in the deficiencies described here. Nevertheless, the tropical stability, obtained with no flux correction, appears robust. It is an encouraging feature for long term climate simulations.

References

Barkstrom BR (1984) The Earth Radiation Budget Experiment (ERBE). Bull Am Meteorol Soc 65:1170–1185

Blanke B, Delecluse P (1993) Low frequency variability of the tropical Atlantic ocean simulated by a general circulation model with mixed layer physics. J Phys Oceanogr 23:1363–1388

Boer GJ, Arpe K, Blackburn M, Déqué M, Gates WL, Hart TL, Le Treut H, Roeckner E, Sheinin DA, Simmonds I, Smith RNB, Tokioda T, Wetherald RT, Williamson D (1992) Some results from an intercomparison of the climates simulated by 14 atmospheric general circulation models. J Geophys Res 97(D12): 12771–12786

Bougeault P (1985) A simple parametrization of the large-scale effect of deep cumulus convection. Mon Weather Rev 113:2108–2121

Bryan K, Manabe S, Spelman MJ (1988) Interhemispheric asymetry in the transient response of a coupled ocean-atmosphere model to CO2 forcing. J Phys Oceanogr 18:851–867

Cubasch U, Hasselman K, Höck H, Maier-Reimer E, Mikolajewicz U, Santer BD, Sausen R (1992) Time-dependent greenhouse warming computations with a coupled ocean-atmosphere model. Clim Dyn 8:55–69

Dandin P (1993) Variabilité basse fréquence simulée dans l'océan Pacifique Tropical. PhD Thesis Université Paris 6-France

Delecluse P, Madec G, Imbard M, Levy C (1993) OPA version 7 ocean general circulation model reference manual. LODYC, Intern Rep 93/05

Déqué M, Dreveton C, Braun A, Cariolle D (1994) The ARPEGE/IFS atmosphere model: a contribution to the French community climate modelling. Clim Dyn 10:249–266

England MH (1993) Representing the global-scale water masses in ocean general circulation models. J Phys Oceanogr 23:1523–1552

Esbensen SK, Kushnir V (1981) The heat budget of the Global Ocean: an atlas based on estimates from marine surface observations. Climatic Research Institution 29, Oregon State University, Corvallis, OR, USA

Gates WL (1992) AMIP: The Atmosphere Model Intercomparison Project. Bull Am Meteorol Soc 73:1962–1970

Gates WL, Han YJ, Schlesinger ME (1985) The global climate simulated by a coupled atmosphere-ocean general circulation model: preliminary results. In: Coupled ocean-atmosphere models, JCJ Nihoul (ed) Elsevier, Amsterdam, pp 131–151

Gates WL, Cubasch U, Meehl GA, Mitchell JFB, Stouffer RJ (1993) An intercomparison of selected features of the control climate simulated by coupled ocean-atmosphere general circulation models. WCRP-82, WMO/TD-574

Geleyn JF (1987) Use of a modified Richardson number for parametrizing the effect of shalow convection. J Meteorol Soc Japan, special NWP Symp vol:141–149

Geleyn JF, Hollingsworth A (1979) An economical analytic method for the computation of the interaction between scattering and line absorption of radiation. Beit Phys Atmos 52:1–16

Gleckler PJ, Randall DA, Boer G, Colman R, Dix M, Galin V, Helfand M, Kiehl J, Kitoh A, Lau W, Liang XZ, Lykossoz V, McAvaney B, Miyakoda K, Planton S (1994) Cloud radiative effects on implied oceanic energy transports as simulated by atmospheric general circulation models. PCMDI Rep 15, Lawrence Livermore National Laboratory, Livermore, CA

Guilyardi E, Madec G, Terray L, Déqué M, Pontaud M, Imbard M, Stephenson D, Filiberti M-A, Cariolle D, Delecluse P, Thual O (1995) Simulation couplée océan-atmosphère de la variabilité du climat. C R Acad Sci Paris, 320/2a:683–690

Hellerman S, Rosenstein M (1983) Normal monthly wind stress over the world ocean with error estimates. J Phys Oceanogr 13:1093–1104

Le Treut H, Li ZX, Forichon M (1994) Sensitivity of the LMD general circulation model to greenhouse forcing associated with two different cloud water parametrizations. J Clim 7:1827–1841

Levitus S (1982) Climatological Atlas of the world ocean. NOAA Prof Pap 13, pp 173

Louis JF, Tiedke M, Geleyn JF (1982) A short history of the operational PBL-parametrization at ECMWF. In: Proc ECMWF Work shop Planetary Boundary Layer Parametrization, 25–27 November 1981, pp 59–80, ECMWF, Shinfield Park, Reading, UK

Ma CC, Mechoso CR, Robertson A, Arakawa A (1996) Peruvian stratus clouds and the tropical Pacific circulation: a coupled ocean-atmosphere GCM study. J Climate 9:1635–1645

Madec G, Imbard M (1996) A global ocean mesh to overcome the North Pole singularity. Clim Dyn 12:381–388

Madec G, Chartier M, Delecluse P, Crépon M (1991) A three dimensional numerical study of deep water formation in the northwestern Mediterranean Sea. J Phys Oceanogr 21:1349–1371

Mahfouf JF, Cariolle D, Royer JF, Geleyn JF, Timbal B (1994) Response of the Météo-France climate model to changes in CO_2 and sea surface temperature. Clim Dyn 9:345–362

Manabe S, Bryan K (1969) Climate calculations with a combined ocean-atmosphere model. J Atmos Sci 26:786–789

Manabe S, Stouffer RJ, Spelman MJ, Bryan K (1991) Transient responses of a coupled ocean-atmosphere model to gradual changes of atmospheric CO_2. Part I: annual mean response. J Clim 4:785–818

Manabe S, Spelman MJ, Stouffer RJ (1992) Transient responses of a coupled ocean-atmosphere model to gradual changes of atmospheric CO_2. Part II: seasonal response. J Clim 5:105–126

Meehl GA, Washington WM, Semtner AJ Jr (1982) Experiments with a global ocean model driven by observed atmospheric forcing. J Phys Oceanogr 12:301–312

Meehl GA (1990) Development of global coupled ocean-atmosphere general circulation models. Clim Dyn 5:19–33

Meehl GA (1995) Global coupled general circulation models. Scripps Meeting 10–12 October 1994, La Jolla CA. Bull Am Meteorol Soc 76:951–957

Murphy JM (1992) A prediction of the transient response of climate. Climate Research Technical Note 32, Hadley Center for Climate Prediction and Research. Bracknell UK, pp 27

Murphy JM (1995) Transient response of the Hadley Center coupled ocean-atmosphere model to increased carbon dioxide. Part I: control climate and flux adjustment. J Clim 8:36–56

Neelin JD, Dijkstra HA (1995) Ocean-atmosphere interaction and the tropical climatology. Part I: the dangers of flux-correction. J Clim 8:1325–1342

Oberhuber JM (1988) An atlas based on the COADS data set: the budget of heat, buoyancy and turbulent kinetic energy at the surface of the global ocean. Max-Planck-Institut für Meteorologie, Rep 15

Oort AH, Vonder Haar TH (1976) On the observed annual cycle in the ocean-atmosphere heat balance over the Northern Hemisphere. J Phys Oceanogr 6:781–800

Pontaud M (1996) Variabilité interannuelle dans le Pacifique Tropical et instabilités couplées océan-atmosphère. PhD Thesis l'Université Paul Sabatier, Toulouse, France

Pontaud M, Terray L, Guilyardi E, Sevault E, Stephenson DB, Thual O (1995) Coupled ocean-atmosphere modelling: computing and scientific aspects. In: Proc 2nd UNAM-CRAY Supercomputing Conf, 21–24 June 1995, Mexico City, Mexico, Cambridge University Press, to be published

Ramanathan V, Cess RD, Harrison EF, Minnis P, Barkstrom BR, Ahmed E, Hartmann D (1989) Cloud radiative forcing and climate, results from ERBE. Science 243:57–63

Reverdin G, Delecluse P, Lévy C, Morlière A, Verstraete JM (1991) The near surface Atlantic in 1982–1984, results from a numerical simulation and a data analysis. Prog Oceanogr 27:273–340

Reynolds RW (1988) A real-time global sea surface temperature analysis. J Clim 1:75–86

Ritter B, Geleyn JF (1992) A comprehensive radiation scheme for numerical weather prediction models with potential applications in climate simulations. Mon Weather Rev 120:303–325

Rossow WB, Shiffer RA (1991) ISCCP cloud data products. Bull Am Meteorol Soc 72:2–20

Royer JF, Planton S, Déqué M (1990) A sensitivity experiment for the removal of Arctic sea ice with the French spectral general circulation model. Clim Dyn 5:1–17

Sadourny R, Laval K (1984) January and July performances of the LMD general circulation model. In: Berger, A., Nicolis, C. (eds) New perspective in climate modelling. Elsevier, pp 173–198

Stockdale T, Latif M, Burgers G, Wolff J-O (1994) Some sensitivities of a coupled ocean-atmosphere GCM. Tellus 46A:367–380

Terray L (1994) The OASIS coupled user guide version 1.0, CERFACS Tech Rep TR/CMGC/94–33

Terray L, Thual O, Belamari S, Déqué M, Dandin P, Delecluse P, Levy C (1995) Climatology and interannual variability simulated by the ARPEGE-OPA coupled model. Clim Dyn 11:487–505

Timbal B, Mahfouf JF, Royer JF, Cariolle D (1995) Sensitivity to prescribed changes in sea surface temperature and sea ice in doubled carbon dioxide experiments. Clim Dyn 12:1–20

Trenberth KE, Solomon A (1994) The global heat balance: heat transports in the atmosphere and ocean. Clim Dyn 10:107–134

Unesco (1983) Algorithms for computation of fundamental property of sea water, Unesco Techn Pap Mar Sci, 44

Wallace JM (1992) Convective cloud systems and warm-pool SSTs: coupled interactions and self regulation. J Geophys Res 98:12881–12893

Washington WM, Meehl GA (1989) Climate sensitivity due to increased CO_2: experiments with a coupled atmosphere and ocean general circulation model. Clim Dyn 4:1–38

Wessel P, Smith WHF (1991) Free software helps map and display data. EOS Trans Am Geophys Union 72:441, 445–446

Xie P, Arkin PA (1996) Analyses of global monthly precipitation using gauge observations, satellite estimates and numerical model predictions. J Clim 9: (in press)